

# SEEING THROUGH MARITIME FOG USING SENSOR FUSION

Visual Machines Group, UCLA

## ABSTRACT

This report proposes the use of visible-thermal image sensor fusion to image through maritime fog. The state-of-the-art in sensor fusion algorithms are studied from the lens of computer science. In contrast to previous approaches, we lean more heavily on the physics of scattering to solve the inverse problem. Specifically, we move away from the simplified single scattering model as widely used in previous work to formulate a maritime fog forward model which considers blur caused by multiple scattering. Then, this forward model can be used as a Bayesian prior to iteratively fuse images from every spectral channel. Experiments on synthetic data show our method can achieve substantial improvements in the detail recovery and contrast restoration over existing sensor fusion methods for maritime defogging. This lays a foundation for incorporating physics into image processing and machine learning pipelines.

## 1. INTRODUCTION

In this report, we shed light on the mystery of seeing through **maritime fog** using multispectral **sensor fusion**.

Sensor fusion for defogging is not new. For defogging, a widely studied and related area is on-land defogging [1, 2, 3, 4], where the fog is mostly assumed to be thin and the single scattering model is used to model the image formation [1]. Previous sensor fusion approaches have leveraged the single-scatter model. For example, Multi-resolution Image Fusion (MIF) [5] is widely used for defogging by fusing images perceived from multispectral channels **pixel-wise** and has inspired many extensions based on MIF [6, 7, 8].

Unfortunately, maritime fog has an optical phase function and thickness that do not conform to the single scattering model. Here, multiple scattering induces attenuation and blur simultaneously [9, 10, 11] (Fig. 1). The blur leads to model mismatch between the single scattering model and makes the pixel-wise multi-resolution fusion erroneous.

To overcome the above problem, this report studies both the forward and inverse problems as follows:

- **Forward model:** We propose a forward model for image degradation in maritime fog conditions (Sec. 2). This forward model is more realistic than the single scattering model as we additionally consider blur that cannot be ignored in heavy fog situations, such as maritime fog (Fig. 1).

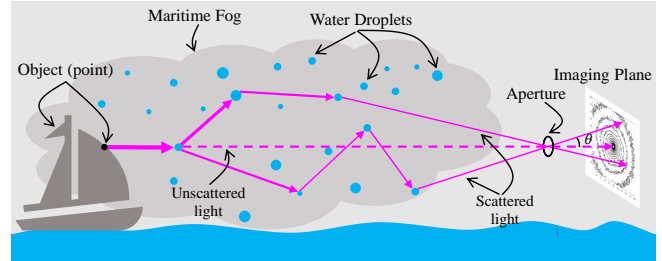


**Fig. 1: Multiple scattering is prevalent in maritime fog.** In maritime fog, dense fog and large water droplets result in multiple scattering. The multiple scattering of light from a point source to a sensor leads to evident image blur.

- **Inverse problem:** We propose a multi-projection fusion algorithm for fusing multispectral bands, to enhance the defogging ability (Sec. 3). The ability of considering blur in our sensor fusion procedure enables our method to achieve a better result than the existing ones.

To our knowledge, this is the first sensor fusion approach that spans both optical phase function characterization and convex image processing. Results support the logic of a hybrid approach between image processing and optics.

## 2. REALISTIC MARITIME FOG MODEL

In this section, we articulate the scattering mechanism that introduces high attenuation and considerable blur into imaging through maritime fog, compared to that of other types of fog/haze. To take account of both factors, we propose a new forward model that also facilitates image reconstruction with sensor fusion.

### 2.1. Transmission of maritime fog

Seeing through maritime fog is a challenging technical problem due to low transmission and considerable blur of objects.

The transmission ratio  $t$  of a light beam through scattering medium is often evaluated with respect to scattering coefficient  $\beta$  and distance of propagation  $d$ :

$$t = e^{-\tau} = e^{-\beta d}, \quad (1)$$

where  $\tau$  is defined as the optical thickness. The scattering coefficient is the sum of extinction and absorption coefficients,

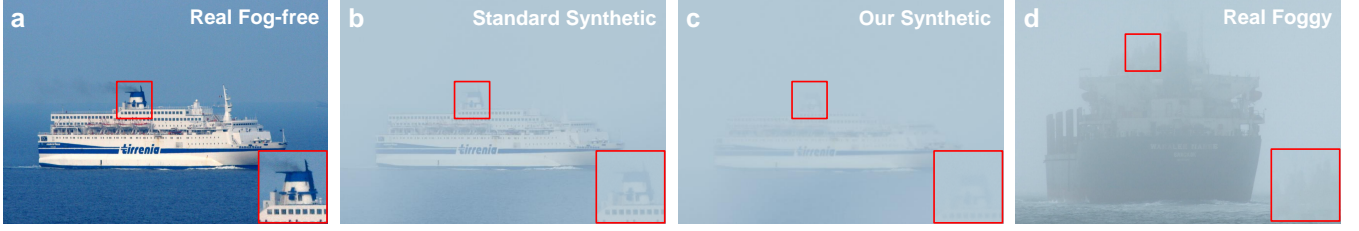


**Fig. 2: The proposed forward model enables more realistic modeling of maritime fog.** (a) Photograph of real scene in clear conditions [12]; (b) Synthetic image from single-scatter forward model [1]; (c) Synthetic image from our proposed forward model; (d) Photograph of real maritime fog [13]. By simulating the maritime fog with a similar blur effect as in real foggy images (d), we obtain a more realistic synthetic image (c), validating our forward model (Subsection 2.3).

i.e.  $\beta = \beta_{ext} + \beta_{abs}$ . Usually,  $\beta_{abs}$  can be ignored in water-droplet-based fog in general. For maritime fog, due to higher concentration of inorganic ions, sulfate and nitrate [14], the average refractive index of molecules tend to have a non-zero imaginary part which increases the absorption coefficients. On the other hand, light through maritime fog usually has larger distance of travel  $d$  because of the geometric features of the scene. Therefore, the optical thickness  $\tau$  is larger and the transmission ratio  $t$  is smaller than terrestrial fog in general. Equation 1 will be adopted in our model to emulate the attenuation of light in maritime fog.

## 2.2. Multiple scattering in maritime fog

Apart from attenuation of direct transmission, it is necessary to consider multiple scattering in maritime fog. We verify it by evaluating the mean free path (MFP). The mean free path quantifies the average distance traveled by the photons between two consecutive scattering events. It is defined as:

$$MFP = \frac{1}{\beta}. \quad (2)$$

Therefore, photons in maritime fog travels shorter distance and are scattered more frequently within unit distance. This multiple scattering introduces considerable blur into maritime images.

**Phase function** Phase function is important in analysing scattering as it describes the angular distribution of light intensity scattered by a particle. The phase function for maritime fog is related to the droplet size distribution  $n(r)$  of maritime fog where  $r$  is the droplet radius. Without burdening the complexity of measuring real world data, we verify that the  $\Gamma$ -distribution fits well with real data. Equations and plots are shown in Section A in Appendix. Since the theoretical distribution is accurate, we proceed with it to derive a phase function

$$P_{maritime}(\theta, \phi) = \int_1^{50} n(r) P_{mie}(x, \theta, \phi) dr, \quad (3)$$

where  $n(r)$  is the normalized distribution,  $x = \frac{2\pi r}{\lambda}$ ,  $\lambda$  is the wavelength. The simulated phase function is plotted in

Fig. 3. We can see that the phase function of maritime fog has a smaller scattering angle in contrast to haze phase function. Intuitively speaking, this characteristic makes blur more apparent in maritime fog. Light scattered by haze aerosols, tends to have wide angles relative to the original propagation direction. Here, we assume a relatively large distance between objects and the imaging plane (i.e. maritime are photographed from far away—ships covered by the fog, are far away from the camera). Because the angle subtended by the camera and objects is small, only limited scattered photons reach the image plane. The intensity profile of scattered light is too wide to be observed as a separate entity with ordinary optics [15, 10]. However, with fog droplets, the scattering angle is small relative to the initial direction of propagation. This results in an appreciable amount of forward scattered radiation in addition to the ballistic photons [16, 17, 18].

What matters in phase function is the ratio of particle size and wavelength, instead of the absolute value of each of them. If we take a limit of  $x = \frac{2\pi r}{\lambda}$ , i.e.

$$\lim_{x \rightarrow X} P_{maritime}(\theta, \phi), \quad (4)$$

phase function can be well approximated by the Rayleigh scattering if  $X$  is small enough (e.g. in thermal imaging). The scattering coefficient  $\beta$  also decreases drastically, leading to clear and sharp images. However, when  $X$  is too large, the scattering mechanism has to be explained by the geometric optics.

**PSF Analysis** To achieve our eventual goal of using physical insights in the inverse problem, we must mathematically characterize the blurring. We do so here, assuming a diffraction-limited lens with limited aperture size.

We use factorial analysis, combined with our experimental results (Appendix Sec. C), to formulate an empirical model of the blur PSF as a function of two factors, i.e., optical thickness  $\tau$  and the wavelength  $\lambda$ . The PSF profile of light in scattering media is given by:

$$PSF(\theta) = I_{bal}(\theta) + I_{sca}(\theta), \quad (5)$$

where  $\theta$  is angle of light incident onto the camera,  $I_{bal}$  is the intensity of ballistic light components,  $I_{sca}$  is the intensity

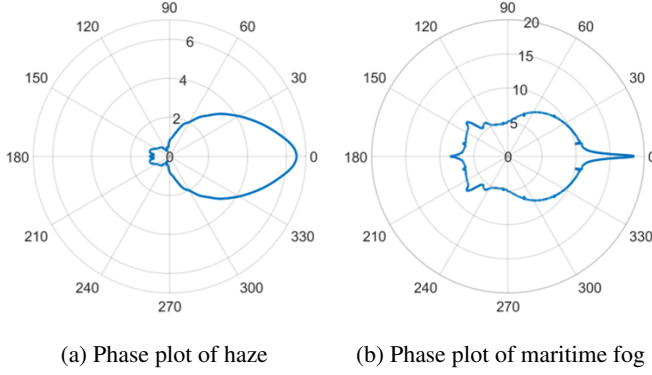


**Fig. 3: A comparison between phase plots of haze and fog shows that fog has smaller scattering angle in general at the visible wavelength.**

of scattered (diffuse) components. In foggy conditions, the ballistic light intensity  $I_{bal}$  is further decomposed as

$$I_{bal}(\tau, \theta) = I_0 \exp(-\tau) \delta(\theta), \quad (6)$$

where  $I_0$  is the intensity under clear weather,  $\tau$  is the optical thickness,  $\delta(\cdot)$  is the impulse function.

The calculation of scattered light requires solving the radiative transfer equation (RTE):

$$\begin{aligned} \mu \frac{\partial I}{\partial \tau} + \frac{1 - \mu^2}{\tau} \frac{\partial I}{\partial \mu} = \\ -I + \frac{1}{4\pi} \int_0^{2\pi} \int_{-1}^{+1} P_{maritime}(\phi', \mu') I d\mu' d\phi', \end{aligned} \quad (7)$$

where  $\mu(\cdot) = \cos(\theta(\cdot))$ . We turn to decomposition of the scattered light intensity  $I_{sca}$  building upon a fast approximation proposed by [11]. Assuming incoherent light, the scattering pattern can be calculated as

$$I_{sca}(\tau, \mu) = \sum_{m=0}^{\infty} (g_m(\tau) + g_{m+1}(\tau)) L_m(\mu), \quad (8)$$

where  $\tau$  is the optical thickness,  $\mu = \cos(\theta)$ ,  $g_m(\tau)$  computes the attenuation and  $L_m(\mu)$  is the Legendre polynomial that characterizes angular spread due to multiple scattering, associated with the phase function we derived before.

Putting this together, if we consider an imaging system with aperture diameter  $D$  and focal length  $f_l$ , the PSF at the imaging plane is given as

$$PSF(\theta) = \frac{k^2}{(2\pi f_l)^2} (\pi a^2)^2 \left\{ I_{bal}(\theta) + \frac{1}{\pi} \left( \frac{\lambda}{a} \right)^2 I_{sca}(\theta) \right\}, \quad (9)$$

where  $a$  is the average droplet size, and  $\lambda$  is the wavelength [19].

As  $\tau$  becomes larger, both ballistic and scattered light get attenuated. Moreover, the scattered intensity profile broadens

as a result of smaller MFP. As the particle size  $a$  increases, the cutoff frequency of the Modulation Transfer Function (MTF) increases. The cutoff frequency here is defined as the frequency where the MTF magnitude equals one-half of its total drop due to multiple scattering. A theoretical equation for the cutoff frequency is  $f_c = \frac{a}{\lambda f_l}$  [15]. For maritime fog, the droplet size stays within the range that the blurring effect is visually obvious. Therefore, a new forward model that emulates the blur from multiple scattering of maritime fog is necessary.

### 2.3. Maritime fog formation model

After disclosing the blurring effect and deriving the PSF in previous subsections, we formulate the forward model specifically for maritime fog, shown as:

$$I(x) = J(x) t(x, \tau) * PSF(\lambda, \tau) + A(1 - t(x, \tau)), \quad (10)$$

where  $I$  is the captured image,  $J$  is the scene radiance,  $A$  is the global atmospheric light, and  $t$  is the medium transmission describing the portion of ballistic light, varying with the change of optical thickness  $\tau$ .

Assuming that the foggy atmosphere is homogeneous, the transmission  $t$  is:

$$t(x) = e^{-\beta(\lambda) d(x)}, \quad (11)$$

where  $\tau = \beta(\lambda) d(x)$ ,  $d(x)$  is the depth map of the scene,  $\beta$  is the scattering coefficient of the atmosphere, varying with the wavelength  $\lambda$ , i.e.,  $\beta(\lambda) = \frac{\text{constant}}{\lambda^n}$  where  $n$  varies from 0.7 to 4. This aligns with Eq. 6 in previous analysis.

To validate the forward model, we simulate the synthetic maritime foggy image based on our forward model and compare it with both the real maritime foggy image and the result synthesized from single scattering only. The comparison is displayed in Fig. 2. As is clearly shown, the image generated by our forward model looks more realistic with blurry edges and highly reduced contrast.

The forward model here also discloses two key features regarding multispectral recordings. It indicates that: on the one hand, the larger the recorded wavelength is, the higher the transmission  $t$ ; on the other hand, multispectral data provides differential contrast over the spectral bands. Besides, due to high cost in manufacturing process, IR cameras usually have lower resolution compared to RGB camera. Thus, it is desired to develop a fusion algorithm to fuse all wavelength bands to enhance visibility and resolution of imaging through fog.

## 3. MULTI-PROJECTION SENSOR FUSION

In this section, we first describe the reconstruction algorithm (Subsection 3.1) and then demonstrate our algorithm outperforms the existing ones. (Subsection 3.2).

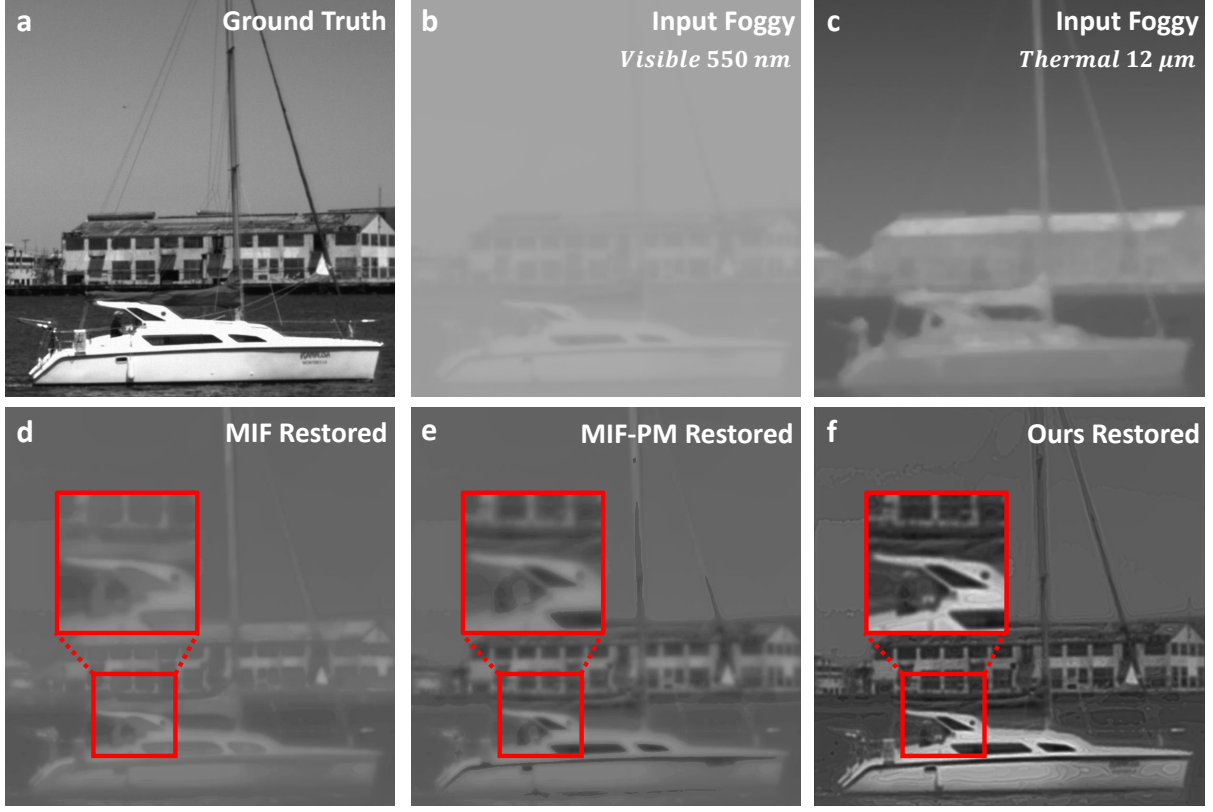


**Fig. 4: Reconstruction result from multi-projection fusion shows an enhancement as compared to the existing methods.** From top to bottom, right to left are ground truth (a), synthesized input visible (b) and thermal foggy (c) images, original MIF fusion (d), upgraded MIF-PM fusion (e) and our multi-projection fusion (f) results. Our method performs the best in retrieving the edges and contrast.

### 3.1. Algorithm description

Following the investigation above, we propose a multi-projection sensor fusion algorithm to exploit the merits of all spectral bands and take the blur into consideration, so as to achieve the defogging goal. The proposed fusion framework is inspired by an extensive body of work on solving inverse problems in imaging via maximum-a-posteriori (MAP) estimation under a Bayesian model. The forward model in Subsection 2.3 could be abstracted as  $I = \mathcal{A}_\lambda(J)$ . We formulate here that all the recordings (i.e., recordings from all the color channels)  $\{I_i\}_{i=1}^N$ , are the projections of ground truth, through certain transformations.  $N$  here is the number of multispectral channels. Specifically, in the case of multispectral recordings, the transformation is the combination of the forward model (single scattering + blur) and the color filtering.

When it comes to single projection, the probabilistic model for a projection is  $P(I, J) = P(I|J)P(J)$ . Compared to the single projection setting, we have a set of projections  $V = \{v_1, v_2, \dots, v_N\}$  comprising  $N$  observed distributions  $\{I_{v_i}(x, \lambda_{v_i})\}_{i=1}^N$  (input projections acquired from differ-

ent physical conditions, such as images of different spectral channels from a multispectral camera). The goal is to maximize the probability of reconstructing the underlying  $J(x)$  (the object reflectance) given the acquired observations  $\{I_{v_i}(x, \lambda_{v_i})\}_{i=1}^N$ . Such a problem is usually dubbed as MAP. According to Bayes' theorem, it is expressed as:

$$P(J|I_{v_1}, I_{v_2}, \dots, I_{v_N}) = \frac{P(I_{v_1}, I_{v_2}, \dots, I_{v_N}|J)P(J)}{P(I_{v_1}, I_{v_2}, \dots, I_{v_N})}, \quad (12)$$

where the denominator  $P(I_{v_1}, I_{v_2}, \dots, I_{v_N})$  is the evidence probability which is a constant. The optimization procedure is jointly maximizing the data likelihood and prior probability. The latter term  $P(J)$  relates to the prior distribution about the object  $J$ , which can be represented by the regularization of the object. Applying the negative log onto Eq. 12, we derive the objective function:

$$\hat{J} = \arg \min_J \sum_{i=1}^N \|A(\lambda_{v_i})J - I_{v_i}\|_2^2 + R(J), \quad (13)$$

where the data term  $\sum_{i=1}^N \|A(\lambda_{v_i})J - I_{v_i}\|_2^2 = -\log P(I_{v_1},$



**Algorithm 1** Multi-projection sensor fusion**Input:**

Recordings  $\{I_{v_i}\}_{i=1}^N$ , forward models  $\{\mathcal{A}_{v_i}\}_{i=1}^N$ , maximum iterations  $K$ .

**Output:**

Optimized  $J$

- 1: **Initialization:** Initialize both  $J_0$ , a rough estimate of ground truth and  $I_{vis}$  as  $DCP(I_{vis})$ .
- 2: **for**  $k = 0$  to  $K$  **do**
- 3:    $\hat{J}_k \leftarrow \arg \min_J \sum_{i=1}^N \|I_{v_i} - \mathcal{A}_{v_i} J\|_2^2$
- 4: **end for**
- 5: **return**  $J = \hat{J}_k$

	MIF [5]	MIF-PM [6]	Ours*	Ours
PSNR	14.0418	14.5957	14.5927	<b>15.0655</b>
SSIM	0.6972	0.7349	0.7475	<b>0.7709</b>

**Table 1: Quantitative PSNR/SSIM results of different sensor fusion approaches.** The best model is marked in **red**. Our method wins out on both PSNR and SSIM. Ours\* denotes ablated version of our method without considering the blur.

$I_{v_2}, \dots, I_{v_N}|J)$  and the prior term  $R(J) = -\log P(J)$  are negative log-likelihoods.

**Implementation details** Same as in MIF [5], our goal is to optimize the estimate of the object’s reflectance  $J$  (corresponding to the gray-scale images), which determines the visibility for seeing through maritime fog.

The recovery algorithm is detailed in Algorithm 1. Since we feed Thermal and Visible data as the input into the algorithm,  $\{I_{v_i}\}_{i=1}^N$  corresponds to Visible foggy recording  $I_{vis}$  and Thermal foggy recording  $I_{thermal}$ .  $\{\mathcal{A}_{v_i}\}_{i=1}^N$  are their forward models, which differ with each other by wavelength. In our implementation, we don’t add regularization onto the algorithm.

Moreover, in our implementation, we manually tune the rough estimate of PSFs based on the fact that an overly large PSF leads to blur while an overly small PSF leads to the ringing effect. Particularly, in the initialization stage, we utilize Dark Channel Prior (DCP) [2] method to pre-process  $I_{vis}$  and set its output as both  $J_0$  (the initialization of  $J$ ) and updated  $I_{vis}$ . This procedure is shown in step 1, Algorithm 1.

### 3.2. Reconstruction evaluation

In this subsection we show that our sensor fusion result is better than existing methods for defogging through maritime fog.

As there doesn’t exist a real foggy dataset taken with multispectral cameras, we utilize the method described in Subsection 2.3 to synthesize maritime foggy images for both Visible

and Thermal bands. The fog-free Visible and Thermal images are from VAIS dataset [20], which to the best of our knowledge, is the only open-source dataset for maritime multispectral imaging. We apply the multi-projection sensor fusion

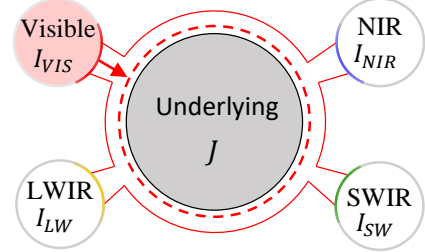


**Fig. 5: A conceptual sketch of multi-projection sensor fusion method.** In sensor fusion, every recording  $\{I_{VIS}, I_{NIR}, \dots\}$  is essentially a projection of the underlying ground truth  $J$  through certain physical process (e.g., color filtering). According to Bayes’ theorem, in every sub-iteration, our method takes the intermediate estimate  $\hat{J}$  output from other projections and updates the estimate of  $J$  based on both  $\hat{J}$  and current projection.

onto our synthetic images. We evaluate the recovered image by comparing it with the widely adopted MIF fusion, and its very recent upgraded version MIF & Probability Map (MIF-PM) [21]. The latter improves upon MIF by additionally considering a probabilistic inconsistency map between different spectral channels. As mentioned previously, the MIF method uses the luminance of Visible and Near-infrared (NIR) foggy images as two inputs and fuses the Visible and NIR bands by comparing the contrast of each decomposition pixel-wise. For the sake of making a fair comparison, we replace the foggy recording  $I_{vis}$  with the DCP output  $DCP(I_{vis})$  as the input for both MIF. This is the same as what we have done in the initialization stage of Algorithm 1.

As can be seen from Fig. 4, our restored image possesses not only natural contrast but also sharp details like edges and corners. Even though we replace the Visible foggy image with the DCP-defogged image as the input, the MIF-based methods still perform poorly because of their lack of adaptability to the convolution operation induced by the blur. The quantitative comparison is shown in Table 1, where our multi-projection reconstruction method achieves the highest Peak Signal-to-Noise Ratio (PSNR) and Structural SIMilarity (SSIM). As shown in the table, we also conduct the ablation test onto our method. The ablated version is the one without considering the blur. The results indicate that if we do not take blur into consideration, the result will be of similar quality as MIF-PM.

## 4. DISCUSSION

### 4.1. Conclusion

In summary, we demonstrate that our method outperforms existing ones on seeing through maritime fog. Experimental and synthetic data substantiate that our forward model is more realistic in modeling maritime fog as compared to the single scattering model. The reconstructed results show that our multi-projection fusion algorithm can better fuse Visible + Thermal information and achieve more natural contrast and sharpness than existing methods.

Though we only show the fusion results of Visible + Thermal, our multi-projection sensor fusion could be generalized to all spectral bands. We will continue working on that and show it in future work.

### 4.2. Future work

In this report, we show a preliminary result of our work. There remains great potential in solving maritime defogging in the aspects of the model, algorithm and data.

**Model** The maritime fog formation model is complex. It relates to light scattering, turbulence [22, 23, 24] and many other unknown factors. For example, atmospheric turbulence also plays an important role in maritime fog imaging. The mixture of different eddies involves in maritime fog formation and results as turbulence. The atmospheric turbulence introduces a more random blur into the images. In this report, we derive an empirical model of the PSF. In the future, we will dive deeper into the physical modeling using first principles. Another promising direction is *physics-based learning*, where our group has successfully blended diverse physics priors with deep neural networks [25, 26]. We would utilize the *physics-based learning* to help understand the fog model.

**Algorithmic inversion** We will also utilize *physics-based learning* for solving the inverse problem for such tasks. For seeing through maritime fog, following the multi-projection methodology here, we can build an unrolled network and feed images of multispectral bands into each building block. We can further use physics based neural architecture search method [25] to perfect the network.

**Dataset** We will also build the dataset for this task. Currently, there is no dataset for maritime defogging, no dataset for multispectral sensor fusion, and even no real training dataset for on-land single image dehazing [27]. The deficiency of dataset impedes the progress of not only learning-based but also traditional methods. We will collect a real dataset for: validating and further developing the realistic forward model and training a *physics-based learning* sensor fusion network.

Fortunately, the location of UCLA provides great advantages for us to collect abundant real maritime fog images at the Santa Monica beach or from coastal hiking spots like Los Leones. Equipment such as multispectral Cameras, thermal IR Camera, and tripod will be used. Table 2 lists all the

Description	Qty.	Model	Manufacturer
RGB Camera	1	EOS80D	Canon
50mm Lens for RGB Camera	1	EF 50mm f/1.8 STM	Canon
Multispectral Camera*	1	PixelCam OEM	PIXELTEQ
Fog Machine	1	—	AGPiTEK
Fog Chamber	1	—	—
Optical Table	1	—	Newport
Tripod	1	—	—
Mounted Achromatic Doublets*, f = 30mm	4	AC050-003-B-ML	Thorlabs
Mounted Achromatic Doublets*, f = 50mm	4	AC050-005-B-ML	Thorlabs
Mounted Achromatic Doublets*, f = 150mm	4	AC050-015-B-ML	Thorlabs
Protected Silver Mirrors*	20	—	Thorlabs
Kinematic Glue-In Mirror Mounts*	10	POLARIS-K05G4	Thorlabs
HeNe laser, 632.8nm, 20mW*	1	HNS-20P-633	Meredith Instruments
Mounted LEDs*	1	M405LP1	Thorlabs
DC power supply*	3	TP3005T	Thorlabs

**Table 2: List of parts for collecting real maritime fog images and in-lab foggy images.** \* denotes tentative hardware parts.

used/tentative hardware components for collecting real data or establishing an in-lab platform.

## 5. REFERENCES

- [1] Srinivasa G Narasimhan and Shree K Nayar, “Vision and the atmosphere,” *International journal of computer vision*, vol. 48, no. 3, pp. 233–254, 2002. 1, 2, 8
- [2] Kaiming He, Jian Sun, and Xiaoou Tang, “Single image haze removal using dark channel prior,” *IEEE transactions on pattern analysis and machine intelligence*, vol. 33, no. 12, pp. 2341–2353, 2010. 1, 5
- [3] Codruta Orniana Ancuti and Cosmin Ancuti, “Single image dehazing by multi-scale fusion,” *IEEE Transactions on Image Processing*, vol. 22, no. 8, pp. 3271–3282, 2013. 1
- [4] Wenqi Ren, Si Liu, Hua Zhang, Jinshan Pan, Xiaochun Cao, and Ming-Hsuan Yang, “Single image dehazing via multi-scale convolutional neural networks,” in *European conference on computer vision*. Springer, 2016, pp. 154–169. 1
- [5] Lex Schaul, Clément Fredembach, and Sabine Süsstrunk, “Color image dehazing using the near-infrared,” in *2009 16th IEEE International Conference on Image Processing (ICIP)*. IEEE, 2009, pp. 1629–1632. 1, 5
- [6] Frederike Dümbgen, Majed El Helou, Natalija Gucevska, and Sabine Süsstrunk, “Near-infrared fusion for photorealistic image dehazing,” *Electronic Imaging*, vol. 2018, no. 16, pp. 321–1, 2018. 1, 5
- [7] Chang-Hwan Son and Xiao-Ping Zhang, “Near-infrared image dehazing via color regularization,” *arXiv preprint arXiv:1610.00175*, 2016. 1

- [8] Ashish V Vanmali and Vikram M Gadre, “Visible and nir image fusion using weight-map-guided laplacian–gaussian pyramid for improving scene visibility,” *Sādhanā*, vol. 42, no. 7, pp. 1063–1082, 2017. 1
- [9] Luc R Bissonnette, “Multiscattering model for propagation of narrow light beams in aerosol media,” *Applied optics*, vol. 27, no. 12, pp. 2478–2484, 1988. 1
- [10] Luc R Bissonnette, “Imaging through fog and rain,” *Optical Engineering*, vol. 31, no. 5, pp. 1045–1053, 1992. 1, 2
- [11] Srinivasa G Narasimhan and Shree K Nayar, “Shedding light on the weather,” in *2003 IEEE Computer Society Conference on Computer Vision and Pattern Recognition, 2003. Proceedings.* IEEE, 2003, vol. 1, pp. I–I. 1, 3
- [12] “Pxhere,” <https://pxhere.com/fr/photo/1125657>. 2
- [13] CATHERINE L. BERCHOK, “New discoveries from passive acoustic monitoring and future applications and directions for its use,” <https://www.mmc.gov>. 2
- [14] Darko Koračin, Clive E Dorman, John M Lewis, James G Hudson, Eric M Wilcox, and Alicia Torregrosa, “Marine fog: A review,” *Atmospheric Research*, vol. 143, pp. 142–175, 2014. 2
- [15] NS Kopeika, “Imaging through the atmosphere for airborne reconnaissance,” *Optical Engineering*, vol. 26, no. 11, pp. 261146, 1987. 2, 3
- [16] NS Kopeika, S Solomon, and Y Gencay, “Wavelength variation of visible and near-infrared resolution through the atmosphere: dependence on aerosol and meteorological conditions,” *JOSA*, vol. 71, no. 7, pp. 892–901, 1981. 2
- [17] Yasuo Kuga and Akira Ishimaru, “Modulation transfer function and image transmission through randomly distributed spherical particles,” *JOSA A*, vol. 2, no. 12, pp. 2330–2336, 1985. 2
- [18] LP Volnistova and AS Drofa, “Quality of image transmission through light-scattering materials,” *Optics and Spectroscopy*, vol. 61, pp. 76–79, 1986. 2
- [19] Sermsak Jaruwatanadilok, Akira Ishimaru, and Yasuo Kuga, “Optical imaging through clouds and fog,” *IEEE Transactions on Geoscience and remote Sensing*, vol. 41, no. 8, pp. 1834–1843, 2003. 3
- [20] Mabel M Zhang, Jean Choi, Kostas Daniilidis, Michael T Wolf, and Christopher Kanan, “Vais: A dataset for recognizing maritime imagery in the visible and infrared spectrums,” in *Proceedings of the IEEE Conference on Computer Vision and Pattern Recognition Workshops*, 2015, pp. 10–16. 5
- [21] Frederike Dümbgen, Majed El Helou, Natalija Gucevska, and Sabine Süsstrunk, “Near-infrared fusion for photorealistic image dehazing,” *IS&T Electronic Imaging: Proceedings*, pp. 321–1–321–5(5), 2018, First two authors have equal contribution. 5
- [22] Chang Ki Kim and Seong Soo Yum, “Turbulence in marine fog,” in *Marine Fog: Challenges and Advancements in Observations, Modeling, and Forecasting*, pp. 245–271. Springer, 2017. 6
- [23] Kevin R Leonard, Jonathan Howe, and David E Oxford, “Simulation of atmospheric turbulence effects and mitigation algorithms on stand-off automatic facial recognition,” in *Optics and Photonics for Counterterrorism, Crime Fighting, and Defence VIII*. International Society for Optics and Photonics, 2012, vol. 8546, p. 85460O. 6
- [24] Kevin R Leonard and Richard L Espinola, “Validation of atmospheric turbulence simulations of extended scenes,” in *Infrared Imaging Systems: Design, Analysis, Modeling, and Testing XXV*. International Society for Optics and Photonics, 2014, vol. 9071, p. 907118. 6
- [25] Yunhao Ba, Guangyuan Zhao, and Achuta Kadambi, “Blending diverse physical priors with neural networks,” *arXiv preprint arXiv:1910.00201*, 2019. 6
- [26] Yunhao Ba, Rui Chen, Yiqin Wang, Lei Yan, Boxin Shi, and Achuta Kadambi, “Physics-based neural networks for shape from polarization,” *arXiv preprint arXiv:1903.10210*, 2019. 6
- [27] Codruta O Ancuti, Cosmin Ancuti, Radu Timofte, Luc Van Gool, Lei Zhang, and Ming-Hsuan Yang, “Ntire 2019 image dehazing challenge report,” in *Proceedings of the IEEE Conference on Computer Vision and Pattern Recognition Workshops*, 2019, pp. 0–0. 6
- [28] J Allen Zak, “Drop size distributions and related properties of fog for five locations measured from aircraft,” 1994. 8
- [29] Motoi Kumai, “Arctic fog droplet size distribution and its effect on light attenuation,” *Journal of the Atmospheric Sciences*, vol. 30, no. 4, pp. 635–643, 1973. 8
- [30] Diran Deirmendjian, “Electromagnetic scattering on spherical polydispersions,” Tech. Rep., RAND CORP SANTA MONICA CA, 1969. 8
- [31] Annalisa Dalmoro, Anna Angela Barba, and Matteo d’Amore, “Analysis of size correlations for microdroplets produced by ultrasonic atomization,” *The Scientific World Journal*, vol. 2013, 2013. 8

## Appendix

	Haze	Onland radiation fog	Maritime fog
Diameter range of particles ( $\mu m$ )	0.1 - 1	5 - 35	7 - 65
Liquid Water Content(LWC, $gm^{-3}$ )	$10^{-3}$	0.11	0.17
Visibility (km)	2 - 5	$\leq 1$	$\leq 1$

**Table 3: Typical properties of fog and haze.** Maritime fog generally consists of water droplets in larger size and has lower visibility. The blur effect in maritime fog is mainly due to the large water droplets.

### A. DROPLET SIZE IN MARITIME FOG

Aerosols in haze are usually within  $0.1-1 \mu m$ , while the droplets in maritime fog are within  $7-65 \mu m$  [28]. Note that the ranges only provide a general description of the particle sizes and may not be suitable for all real cases. Measuring the droplet size in the atmosphere can be extremely difficult due to fluctuating thermodynamic conditions. In previous onsite experiments, droplet size of fog above the Arctic ocean is measured with an optical microscope [29]. Droplets of  $5-10 \mu m$  in radius have the highest density. The density of droplets decreases exponentially as the radius of droplet decreases. For theoretical modeling, one of the most common model for droplet size distribution  $n(r)$  is the modified  $\Gamma$ -distribution [30]:

$$n(r) = Ar^\alpha e^{-\beta r^\gamma}, \quad (14)$$

where  $r$  is the droplet radius,  $A$ ,  $\alpha$ ,  $\beta$ ,  $\gamma$  are parameters that vary with density and types of fog. In this report, we fit real data we have acquired with the theoretical model from [30] and plot it in Fig. 6.

### B. EXPERIMENTAL SIMULATION

We experimentally simulate the maritime fog to investigate its inherit properties. To simulate maritime fog in a controlled manner, we conduct a in-lab experiment with setup as shown in Fig. 7. A fog chamber is built to create a closed environment. A resolution chart or point light source serves as the object behind the fog. We use an ultrasonic atomizer with dilute seawater to generate water droplets with size ranging from several microns to around 30 microns [31]. This is plausible because it matches with the particle size distribution of maritime fog [28]. A Canon EOS80D camera is mounted in front of the chamber to capture the object image.

Here in the right of Fig. 7, we showcase both the fog-free and foggy images we acquire with this setup. Apart from objects like bar pattern and resolution chart used as objects, we also capture point spread function (PSF) in foggy condition. In such experiment, We create a point light source

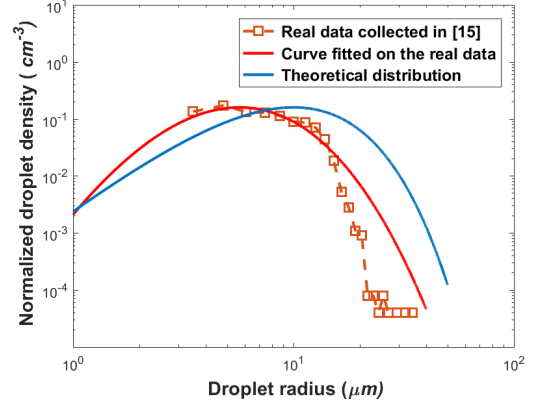


**Fig. 6: Both real measured data and theoretical model reflect that the radii of droplets in maritime fog range from several micrometer to around 50 micrometer.** We apply the fitted curve to generate a phase function specially for maritime fog.

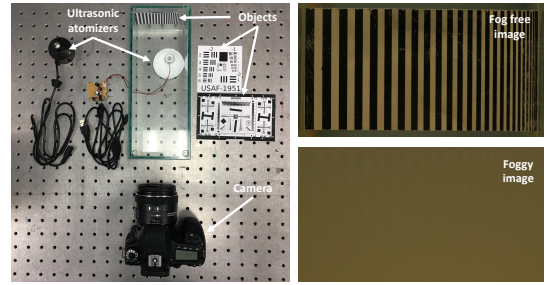


**Fig. 7: Experiment condition for simulating maritime fog.** Left: Experimentally setup for simulating the maritime fog. Right: Real fog-free (upper) and foggy images (lower).

by aligning the center of a small flashlight with the center of a pinhole on a black cardboard. We conduct our experiment in a darkroom where lighting condition is rigorously controlled. The captured PSFs and recordings for maritime fog here is analyzed elsewhere. **Experimental proof of frequency cut-off** We verify the existence of blur effects by showing a clear frequency cutoff in our experimentally simulated dense foggy images. The images are from in-lab experiments detailed in Appendix Sec. B. We conduct a Fourier analysis by taking density profiles along horizontal lines in fog-free and dense foggy images in Appendix Fig. 7 and then applying the Fourier transform. Apart from the magnitude change due to contrast attenuation as indicted in the single scattering model [1], there is clearly a cut-off frequency ( at  $f = \frac{10^2}{1.043 \times 10^{-2}} mm^{-1}$ ) corresponding to the foggy image in Fig. 8. This cut-off frequency phenomenon, resulting from the dense fog, again supports the existence of blur caused by maritime fog.



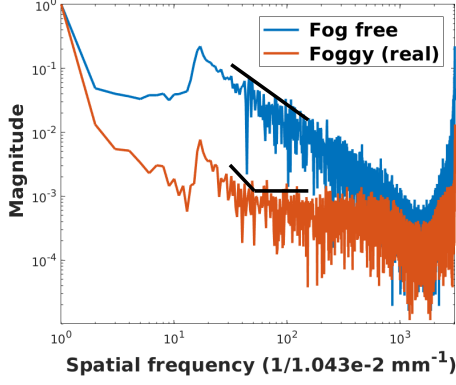


**Fig. 8: Fourier analysis indicates maritime fog has a frequency cut-off, i.e., blur effect.** The cut-off in frequency is indicated by the horizontal line in the figure.

### C. CALIBRATION OF PSF

During the experiment, we calibrate the change of the resulting PSF with respect to the optical thickness  $\tau$ , which is experimentally observed to obey Gamma distribution.

PSF calibration is an alternative to the phase function and Radiative Transfer Equation (RTE) that mathematically describes light transmission in scattering medium. As solving RTE is highly complicated, we model the blur effect by capturing the systematical response to a point light source, i.e. capturing the PSF.

Assuming that ultrasonic atomizer generates fog in a consistent rate, we represent the optical thickness  $\tau$  with time  $t$ :

$$\tau = kt, \quad (15)$$

where  $k$  is a constant. Fig. 9 shows the plot of Full Width at Half Maximum (FWHM) associated with optical thickness. We notice that the FWHM of the PSF shortly increases at the beginning, when fog is below a moderate level. Then it decreases exponentially as the density of fog increases, being almost blocked by fog at the end. Notably, depicted as the orange line in Fig. 9, we empirically find such plot can be further fitted with a gamma distribution  $FWHM_{PSF} \sim f(t|\alpha, \beta)$  as:

$$f(t|\alpha, \beta) = 700 * \frac{1}{\beta^\alpha \Gamma(\alpha)} t^{\alpha-1} e^{-\frac{t}{\beta}}, \quad (16)$$

where  $\Gamma(\alpha)$  is the Gamma Function,  $\alpha = 2.423$  and  $\beta = 17.02$  are parameters that control the shape of the distribution.

Furthermore, after getting the FWHM of the PSFs, we find that the PSFs can be simulated with Cauchy-Lorentz distribution:

$$PSF(x|\gamma) = \frac{1}{\gamma} \frac{\gamma^2}{x^2 + \gamma^2}, \quad (17)$$

where  $\gamma$  controls the shape of the PSF. This is an empirical model of the PSF discovered from our experiments.

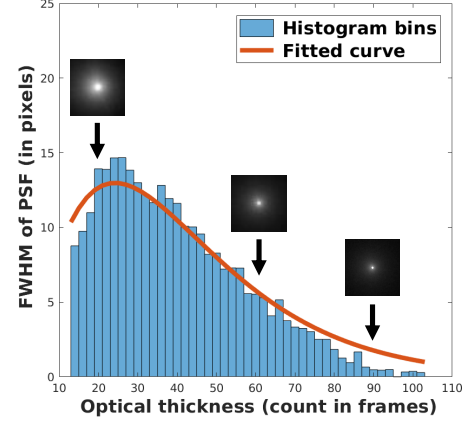


**Fig. 9: FWHM of fog PSF versus the optical thickness obeys a Gamma distribution.** Due to experiment setup, we are unable to measure the absolute optical thickness. Therefore, we measure it by counting the number of passed frames.